Geo-Mar Lett (2011) 31:301–314
DOI 10.1007/s00367-011-0255-x

ORIGINAL

# Topographic control on the nascent Mediterranean outflow

**M. Gasser · J. L. Pelegrí · J. D. Nash · H. Peters · J. García-Lafuente**

Received: 30 September 2010 / Accepted: 15 July 2011 / Published online: 3 August 2011


**Abstract** Data collected during a 12-day cruise in July 2009 served to examine the structure of the nascent Mediterranean Outflow Water (MOW) immediately west of the Espartel Sill, the westernmost sill in the Strait of Gibraltar. The MOW is characterized by high salinities (>37.0 and reaching 38.3) and high velocities (exceeding 1 m s$^{-1}$ at 100 m above the seafloor), and follows a submerged valley along a 30 km stretch, the natural western extension of the strait. It is approx. 150 m thick and 10 km wide, and experiences a substantial drop from 420 to 530 m over a distance of some 3 km between two relatively flat regions. Measurements indicate that the nascent MOW behaves as a gravity current with nearly maximal traveling speed; if this condition is maintained, then the maximum MOW velocity would decrease slowly with distance from the Espartel Sill, remaining significantly high until the gravity current excess density is only a small fraction of its original value. The sharp pycnocline between the Mediterranean and the overlying North Atlantic Central waters is dynamically unstable, particularly where the flow interacts with the 100 m decrease in bottom depth. Here, subcritical gradient Richardson numbers coincide with the development of large interfacial undulations and billows. The very energetic downslope flow is likely responsible for the development of a narrow V-shaped channel downstream of the seafloor drop along the axis of the submerged valley, this probably being the very first erosional scour produced by the nascent MOW. The coincidence of subcritical gradient Richardson numbers with relatively high turbidity values above the channel flanks suggests it may be undergoing upstream erosion.

Responsible guest editor: G. Ercilla

M. Gasser (✉) · J. L. Pelegrí
Departament d’Oceanografia Física,
Institut de Ciències del Mar, CSIC,
08003 Barcelona, Spain
e-mail: gasser@icm.csic.es

J. D. Nash
College of Oceanic and Atmospheric Sciences,
Oregon State University,
Corvallis, OR 97331-5503, USA

H. Peters
Earth and Space Research,
Seattle, WA 98121, USA

J. García-Lafuente
Grupo de Oceanografía Física, Universidad de Málaga,
29071 Málaga, Spain

## Introduction

The Mediterranean Outflow Water (MOW) is born after the Mediterranean Water (MW) passes the Espartel Sill (360 m depth), the westernmost sill in the Strait of Gibraltar (e.g., Madelain 1970; Zenk 1975; Ambar and Howe 1979; Baringer and Price 1999; Habgood et al. 2003; Hernández-Molina et al. 2006; Zitellini et al. 2009; León et al. 2010). The MOW penetrates subsurface layers of the Gulf of Cadiz, driven by pressure gradients caused by the density excess of the intruding MW relative to the ambient North Atlantic Central Water (NACW). This nascent MOW is zonally channeled along the middle slope by the bottom bathymetry, in what constitutes the natural extension of the Strait of Gibraltar, until the channel opens widely into the Gulf of Cadiz. The plunging MOW is an excellent example of a two-way flow–bottom interaction process. The MOW is strongly influenced by the bottom topography, but it is also the principal actor in the development and maintenance of the complex contourite depositional system characterizing the continental slope in the northern gulf sector (e.g., Baraza et al. 1999; Nelson et al. 1999; Habgood et al. 2003; Hernández-Molina et al. 2006; García et al. 2009).

The flow is most intense shortly after exiting the Strait of Gibraltar, as the MW–NACW density difference is maximal here (Baringer and Price 1997a). It is in this energetic, and relatively small, region west of the Espartel Sill that the nascent outflow undergoes its most significant and fastest transformation (Baringer and Price 1997a). The large density-induced MW–NACW velocity difference is responsible for the entrainment of NACW into the MOW, leading to a substantial decrease in salinity and an increase in outflow transport. The mean MOW speed, however, is maintained quite far from this source region (Habgood et al. 2003; Hernández-Molina et al. 2006) because of the transformation of potential into kinetic energy. Therefore, the rate of density transformation of this nascent MOW determines where the current veers northward along the Iberian continental slope, and also its final equilibrium depth.

Paleo-changes in MW density and the depth of the Espartel Sill (relative to sea level) have likely resulted in different MOW paths into the North Atlantic Ocean (Bryden and Stommel 1984), as reflected by the presence of numerous erosional and depositional features of varied ages (Habgood et al. 2003; Hernández-Molina et al. 2006). The MOW erosive activity creates V-shaped downslope scours (Habgood et al. 2003), while the channeling effect helps maintaining high velocities. Increased erosion may locally modify the bottom slope, while accelerating the flow and increasing turbulence, which may lead to an unstable bottom equilibrium slope with an upslope retrogradation of the bottom profile.

Previous oceanographic studies in the region west of the Espartel Sill have paid little attention to the evolution of the MOW in its formation region. An exception is the work of Baringer and Price (1999), who examined the nascent MOW and its relation with depositional bed forms, although at poor spatial resolution (typically about 10 km). In fact, no high-resolution bottom data are available immediately west of the Espartel Sill, precisely where the MOW begins its downwelling path. Only Kenyon and Belderson (1973) characterized the erosional and depositional bed forms at this site, inferred from half a dozen side-scan sonar surveys.

The aim of the present study is to improve our knowledge of flow–bottom interaction along the main outflow channel of the nascent downsloping MOW, based on a novel set of combined oceanographic (CTD and velocity measurements) and bottom topography high-resolution measurements west of the Espartel Sill.

## Physical setting

### Oceanographic setting

When the MOW passes the western Strait of Gibraltar through the Espartel Sill (360 m deep), it initially flows WSW along the axis of the main channel toward the African continent, with a salinity of 38.3 and temperature of 13.3°C under NACW of salinity 36.3 and temperature 15.1°C. The 10-km-wide and 150-m-thick salinity wedge reaches a maximum speed of 1.5 $\mathrm{m\,s^{-1}}$, associated with an excess density of $\Delta\rho$=1.9 kg $\mathrm{m^{-3}}$ (Ambar and Howe 1979; Mulder et al. 2003). The nascent MOW is driven by the downstream pressure gradient generated by this excess density relative to the surrounding fluid (Madelain 1970; Borenäs et al. 2002). Immediately west of the Espartel Sill the flow follows the main channel, but then splits rapidly into different branches (Baringer and Price 1997a), due either to the presence of seamounts or to mixing between MW and NACW. The initial mixing of the MOW is driven largely by local bathymetry-induced acceleration. The flow velocity rises as the bottom slope increases, enhancing vertical shear and favoring subcritical conditions. Shear mixing can result in the rapid formation of two or more layers of different densities (Pelegrí and Sangrà 1998), and these could propagate into the Gulf of Cadiz as distinct cores (Ambar and Howe 1979). Due to such mixing processes, the excess density has decreased enough beyond the 550 m isobath for the Coriolis force to become comparable to the inertial terms, and thus the MOW turns northwest onto the Iberian continental slope (Baringer and Price 1997b).

The distinct MOW cores eventually find their density levels in the northern Gulf of Cadiz (Madelain 1970; Zenk 1975; Ambar and Howe 1979; Ochoa and Bray 1991; Baringer and Price 1999; Borenäs et al. 2002; Serra et al. 2005). Two main cores have been reported. The upper core reaches Cape San Vicente at depths of 500–800 m, with an average speed of about 0.5 $\mathrm{m\,s^{-1}}$, temperature of 13°C, and salinity of 36.2–36.5 (Ambar and Howe 1979; Ambar et al. 1999). The lower core constitutes the main path for MW transport, located at 800–1,200 m and with an average speed of about 0.25 $\mathrm{m\,s^{-1}}$, temperature of 12°C, and salinity of 36.5 (Zenk and Armi 1990; Bower et al. 2002). At this late stage the MOW has lost its gravity current character, and has reached near-geostrophic equilibrium. The exact path along the Iberian slope, however, depends largely on those processes that have modified the outflow density.

### Morphologic setting

MOW impact on sedimentary structures in the northern Gulf of Cadiz has been the subject of many past studies (for a review, see Hernández-Molina et al. 2006). The northeastern sector, located between Cádiz and the Strait of Gibraltar, is a high-velocity zone where multiple scours and sand ribbons have been reported (Baraza et al. 1999; Nelson et al. 1999; Habgood et al. 2003; Hernández-Molina et al. 2006; García et al. 2009), but the region west of the Espartel Sill remains poorly characterized. Here, the MOW flows west, confined by east–west channels (Baringer and Price 1999) and responsible for numerous incisions in the upper sector (400–600 m) of the middle slope (Habgood et al. 2003).

In most of the Gulf of Cadiz, the contouritic systems have the erosional–depositional character of contour flows, or along-slope currents in oceanographic terminology (Baraza et al. 1999; Nelson et al. 1999; García et al. 2009). However, immediately west of the Espartel Sill the nascent MOW has a downslope direction within an east–west submerged valley, hereafter referred to as the Gibraltar Valley. The seafloor is characterized by several ridges acting as barriers and constraining the flow's path, thereby increasing its velocity and erosive potential (Kenyon and Belderson 1973). Habgood et al. (2003) proposed that this nascent downslope MOW is highly erosive, being responsible for the presence of downslope scour alignments, i.e., deep V-shaped channels, along the Gibraltar Valley.

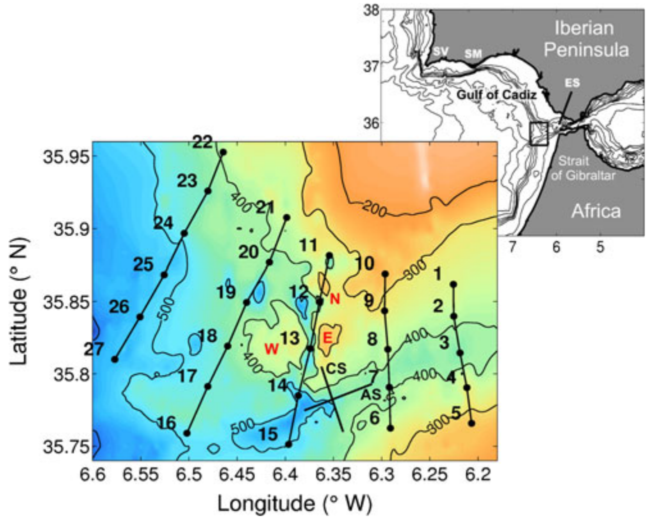


**Fig. 1** Bathymetry based on combined data from the present study, GEBCO and Zitellini et al. (2009), with the locations of the 27 CTD stations and the short along-stream (*AS*) and cross-stream (*CS*) transects: *W* western morphological high, *E* eastern morphological high, *N* northern morphological high. The inset shows a map of the Gulf of Cadiz with bathymetric contours on a 1-min grid from the ETOPO1 data base: *SV* Cape San Vicente, *SM* Cape Santa María, *ES* Espartel Sill, *square* study area

## Materials and methods

Data were collected during a 12-day cruise from 12 to 21 July 2009 on board the R/V García del Cid, in a study area centered at 35.85°N, 6.4°W immediately west of the Espartel Sill (Fig. 1). The cruise started 3 days after the 9 July neap tide and ended 2 days before the 23 July spring tide (Bonanza-Seville tide-recording station, Puertos del Estado, http://www.puertos.es). The study area spans 27× 22 km, examined at 4.5 km resolution; a central area of 5× 5 km was surveyed with an increased resolution of 1 km.

### Bathymetry

The study area is only marginally covered by the high-resolution (250 m) maps available in the compilation by Zitellini et al. (2009). Therefore, additional echo-sounder data were acquired at 1 s intervals with vessel speeds that ranged between 1.5 and 10 knots, and subsequently averaged over 1 min intervals. A gross estimation of the echo-sounder resolution, obtained by using an average ship speed of 6 knots and 1 min-averaged bottom depth data, gives a value of 185 m (square root of study area, 594 km$^2$, divided by the duration of the cruise, 12 days).

The final dataset includes the Zitellini et al. (2009) data, the new echo-sounder data, and the 0.5° resolution General Bathymetric Chart of the Oceans (GEBCO). This set was post-processed and combined using Generic Mapping Tools software to obtain the bathymetry on a 0.1 min grid as shown in Fig. 1. Data density is highest near transects AS and CS (cf. below), and in a 7-km-wide band immediately north of these transects corresponding to the Zitellini et al. (2009) study area.

### In situ measurements

A preliminary survey involving expendable bathythermographs served to determine the approximate path of the MOW. Salinity, temperature, and turbidity data were subsequently acquired at 1 m vertical resolution by means of a Seabird 911Plus CTD at 27 hydrographic stations spaced about 4.5 km apart (Fig. 1, Table 1). Higher-resolution data were acquired in a smaller area in the central channel, and include five continuous fixed-position yo-yo profiles, as well as several short synoptic tow-yo along-stream (AS) and cross-stream (CS) transects repeated over a full tidal cycle and characterizing the phases before and after ebb tide, and before and after flood tide (Fig. 1, Table 1). In the present study, four along-stream and four cross-stream short transects are reported. Tow-yo surveys were carried out at very low ship speeds (1.5 knots) with a vertical cycle wavelength close to 1 km; the total length was 4 km for the cross-stream and 6 km for the along-stream transects, each being completed in less than 2 h.

Continuous current velocities were simultaneously acquired during all surveys, using an RDI Ocean Surveyor 75 kHz

**Table 1** Sampling times and locations for along- and across-stream tow-yo and CTD profiles. Dates correspond to July 2009

| | Initial time (day, hour) | Final time | Initial position | Final position |
|---|---|---|---|---|
| CTD profiles 1–27 | 08, 17:22 | 09, 21:17 | 35°51.71′N, 6°13.53′W | 35°48.60′N, 6°34.61′W |
| Along-stream tow-yo L1 | 09, 23:34 | 10, 00:27 | 35°47.09′N, 6°19.38′W | 35°46.44′N, 6°20.88′W |
| Along-stream tow-yo L2 | 10, 01:50 | 10, 04:01 | 35°47.17′N, 6°18.48′W | 35°45.91′N, 6°22.43′W |
| Along-stream tow-yo L3 | 10, 05:12 | 10, 07:32 | 35°47.41′N, 6°18.49′W | 35°46.30′N, 6°22.11′W |
| Along-stream tow-yo L4 | 10, 08:40 | 10, 10:57 | 35°47.19′N, 6°18.37′W | 35°46.22′N, 6°22.16′W |
| Across-stream tow-yo C1 | 12, 23:41 | 13, 01:34 | 35°45.07′N, 6°20.35′W | 35°47.71′N, 6°21.49′W |
| Across-stream tow-yo C2 | 13, 02:57 | 13, 04:45 | 35°45.14′N, 6°20.42′W | 35°47.92′N, 6°21.60′W |
| Across-stream tow-yo C3 | 13, 06:01 | 13, 07:43 | 35°45.21′N, 6°20.32′W | 35°48.15′N, 6°21.68′W |
| Across-stream tow-yo C4 | 13, 08:43 | 13, 10:14 | 35°45.22′N, 6°20.33′W | 35°48.09′N, 6°21.63′W |

acoustic doppler current profiler (ADCP) in Janus configuration with a theoretical maximum depth range of 750 m. In practice, reliable data reached depths of only about 350–400 m, as near-bottom values were contaminated by sidelobe reflections. Tidal information for the central sector of the study area (near transects AS and CS in Fig. 1) was computed from the ADCP data obtained during the continuous yo-yo surveys covering full tidal cycles, using T-Tide MATLAB routines (Candela et al. 1990; Pawlovicz et al. 2002).

## Flow dynamics

During its initial sinking the MOW is driven by the excess density of MW relative to the surrounding NACW, and so behaves as a gravity current. Under these conditions the MW layer is assumed to flow at the propagation speed of the gravity current head. In the absence of friction, and assuming a negligible slope, this velocity is (Benjamin 1968):

$$v_{\mathrm{gc}} = C(g'd)^{1/2} \tag{1}$$

where $g' = g\Delta\rho/\rho$, i.e., the reduced gravity acceleration, and $C = [(1-\delta)(2-\delta)\delta/(1+\delta)]^{1/2}$, in which $\delta = h/d$, i.e., the ratio between the wedge thickness $h$ and the total water depth $d$. The maximum possible speed of this gravity current is $v_{\mathrm{m}} = 0.53(g'd)^{1/2}$ for $\delta_{\mathrm{m}}$=0.35 (Benjamin 1968; Pelegrí 1988).

The gradient Richardson number (Ri) can be used to assess the dynamic stability of the MOW:

$$\mathrm{Ri} = -\frac{g}{\rho}\frac{\partial\rho/\partial z}{(\partial v/\partial z)^2} \equiv \frac{N^2}{S^2} \tag{2}$$

where $\rho$ is the density, $v$ the along-stream velocity, $z$ the vertical coordinate, and $g$ the gravity acceleration. The buoyancy frequency for an incompressible fluid is defined as

$$N = [-(g/\rho)(\partial\rho/\partial z)]^{1/2} \tag{3}$$

and the along-stream vertical shear as

$$S = \partial v/\partial z \tag{4}$$

For Ri values below some critical value the interfacial waves may become unstable or, equivalently, the flow has enough kinetic energy to provide the required potential energy increase. Some studies argue that this critical value is 0.25, although more recent studies suggest it should be 1 (see Van Gastel and Pelegrí 2004 for a historical perspective).

As mixing takes place, the MOW excess density decreases, so that the speed of the associated gravity current also decreases, and its width increases. The non-dimensional Rossby (Ro) number compares the acceleration and Coriolis force terms, and may be used to evaluate for how long the MOW behaves as a gravity current. $\mathrm{Ro}_y$ and $\mathrm{Ro}_x$ assess the cross-stream ($y$) and along-stream ($x$) force balances, respectively; values much less than 1 indicate that the flow is controlled by the Coriolis force:

$$\mathrm{Ro}_x = \frac{U^2/L_x}{fV} = \frac{U}{fL_y} \tag{5}$$

and

$$\mathrm{Ro}_y = \frac{V^2/L_y}{fU} = \frac{U}{fL_y}\delta^2 \tag{6}$$

where ($L_x$, $L_y$) and ($U$, $V$) are the characteristic length and velocity scales in the ($x$, $y$) directions; $\delta = L_y/L_x$, i.e., the width–length aspect ratio, and the Coriolis parameter is defined as $f$=2Ωsin$\theta$, where Ω is the angular velocity of the Earth and $\theta$ the latitude. The scale relation $U/L_x = V/L_y$ arises from a simple requirement of flow conservation in the horizontal plane.

## Results

### Morphology

Depths in the study area are everywhere over 100 m (Fig. 1), even in the northern sector where nautical charts drawn in the 1970s by the Instituto Hidrográfico de la Marina indicated much shallower values. In the northeastern sector (at about 35.83°N, and 6.32–6.44°W) there is a southward extension of the continental slope with depths of about 300 m, possibly diverting the flow toward the southern part of the study area. South of the continental slope there are three morphological highs with depths of 340 m (southwestern high), 375 m (southeastern high), and 370 m (northeastern high), respectively denoted W, E, and N in Fig. 1.

On the upper continental slope of the western Gulf of Cadiz, the Gibraltar Valley (10 km wide and 150 m deep) stretches approx. zonally from the Strait of Gibraltar until it branches into two main channels (Fig. 1). The northern channel reaches maximum depths of 600 m, with an entrance sill at 325 m. The southern channel increases in depth from 400 to 550 m toward the west, its steepest slopes being in the central sector; in the western part of the AS transect (Fig. 1), the bottom slope increases to 0.1 (seafloor gradient of 5°). The axis of the southern channel between 6.35 and 6.45°W displays a remarkably steep V shape; here, the channel is about 50 m deep and no more than 500 m wide.

### Hydrography

The temperature–salinity diagrams for all CTD records combined (not shown) reveal two well-differentiated water masses: the MW (temperature 13.5°C, salinity 38, potential density 1,030.0 kg $m^{-3}$), and the NACW (temperature 12.5–15°C, salinity 35.75–36.25, potential density 1,028.25 kg $m^{-3}$); the excess density between the MW and the NACW is then 1.75 kg $m^{-3}$. The horizontal distribution of maximum (near-bottom) salinity recorded during the large-scale CTD survey shows the main WSW path of the high-salinity MOW, as well as a flow diversion north of the morphologic low located at 35.8°N, 6.4°W (Fig. 2). The bottom depth increases westward along the MOW core path (cf. dashed white line in Fig. 2), with an abrupt change at about 6.35°W (Fig. 3). The maximum salinities display a general decrease with longitude, the largest change occurring simultaneously with the maximum increase in bottom depth (Fig. 3).

Contrasting with the large-scale difference in vertical salinity patterns between the MW and NACW, changes in turbidity are much more subdued (Figs. 4 and 5). The along-stream cross-section illustrates the existence of near-bottom high-salinity values in excess of 37.5 associated to the MOW path (Fig. 4). The corresponding turbidity values generally increase away from the bottom, except immediately downstream of the abrupt change in bottom depth where a local maximum is present (Fig. 4). Three

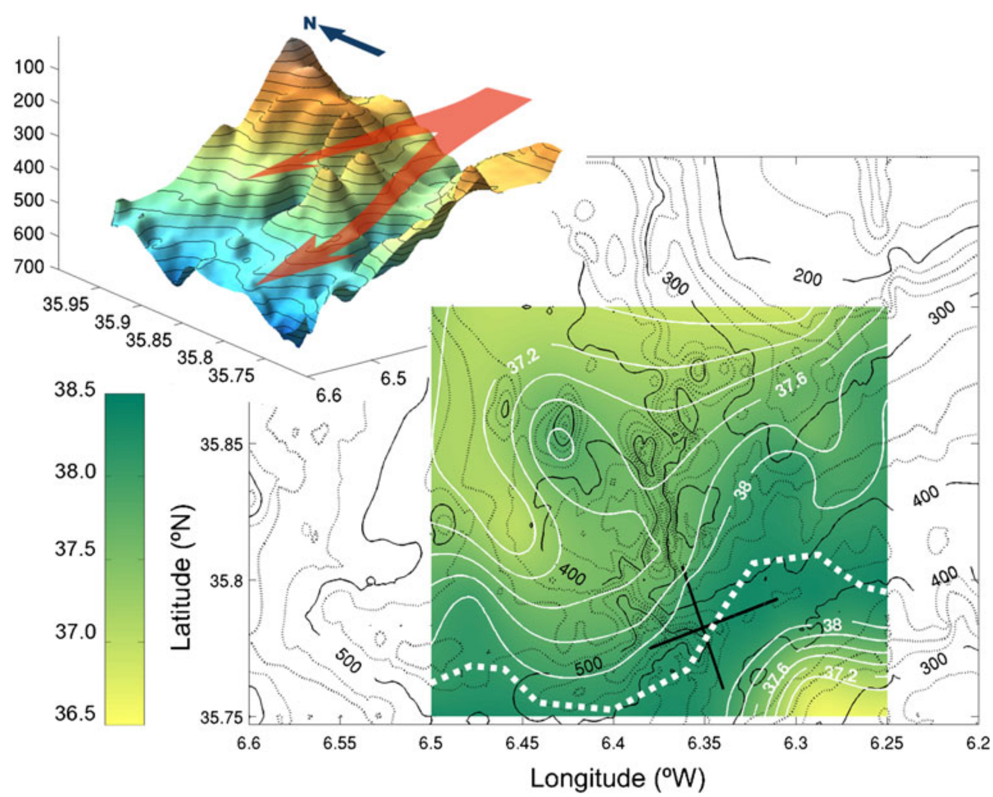


**Fig. 2** Bathymetry (*solid black contours*, in meters) and salinity (*solid white contours* and *green shading*): *dotted white line* maximum salinity values, a proxy for the MOW core path; *straight black lines* locations of the tow-yo cross- and along-stream sections. The inset shows a three-dimensional view of the bottom topography, looking from the southwest: *red arrows* approx. MOW trajectory

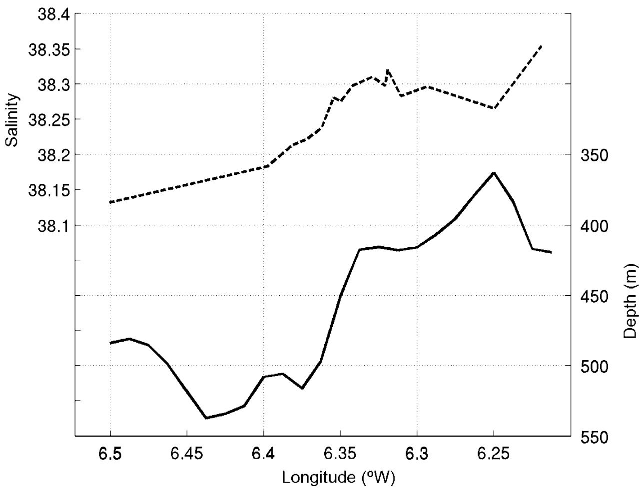


**Fig. 3** Maximum values of salinity (*dashed line*) and bottom depth along the MOW core path (cf. dotted white line in Fig. 2)

meridional cross-sections (at 6.225, 6.35, and 6.5°W) show that only the easternmost one captured the whole width (10 km) of the MOW (Fig. 5), emphasizing the V-shaped bottom profile and clearly defining the track of the high-salinity, low-turbidity MOW.

The M2 tidal velocity component is well aligned with the MOW trajectory (Fig. 6a, b). The tidal velocities are relatively weak (less than 0.2 $ms^{-1}$) within NACW, but increase in the MOW; in fact, the 95% confidence intervals are very large in the lower 150 m, suggesting a substantial tidal effect within the MOW. Figure 6c, d reveals strong temporal variation in the averaged M2 component of the along-stream velocity between 250–350 m over the tidal cycle; note that the duration of each short transect (typically 2 h) is substantially shorter than the characteristic period of the M2 tide (12.4 h).

Distributions of measured (temperature, salinity, turbidity, and velocity) and inferred (buoyancy frequency and gradient Richardson number) parameters on all short transects show large-scale patterns that remain invariable during the different phases of the tidal cycle. In Figs. 7, 8, and 9 depicting the trends for each along-stream transect, L2 and L4 correspond to ebb (out of the strait) and flood conditions, respectively, and L1 and L3 to phases with weaker tidal currents after ebb and flood tide, respectively (cf. Fig. 6). High salinity and turbidity values characterize the MOW, although maximum turbidity is associated to the MW–NACW interface (Fig. 7). Figure 8 shows the corresponding along-stream velocity contours for each but the last along-stream transect, where these data are lacking. There is a depth reversal in the flow direction, whereby the

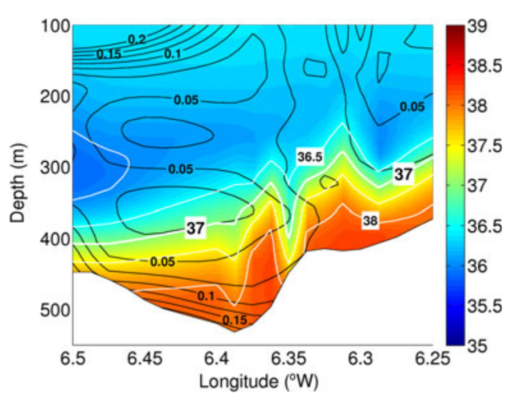


**Fig. 4** Salinity (*white contours* and *color*) and turbidity (*black contours*, FTU units) distributions along the MOW core path (cf. dotted white line in Fig. 2)

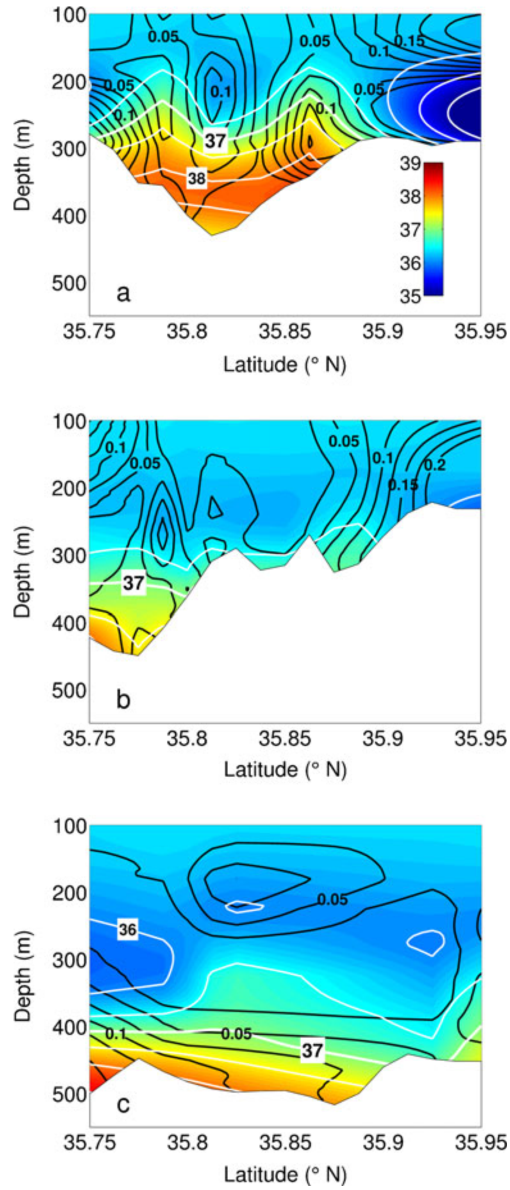


**Fig. 5** Salinity (*white contours* and *color*) and turbidity (*black contours*, FTU units) distributions along the eastern, central, and western meridional large-scale transects at longitudes **a** 6.25°W, **b** 6.35°W, and **c** 6.5°W

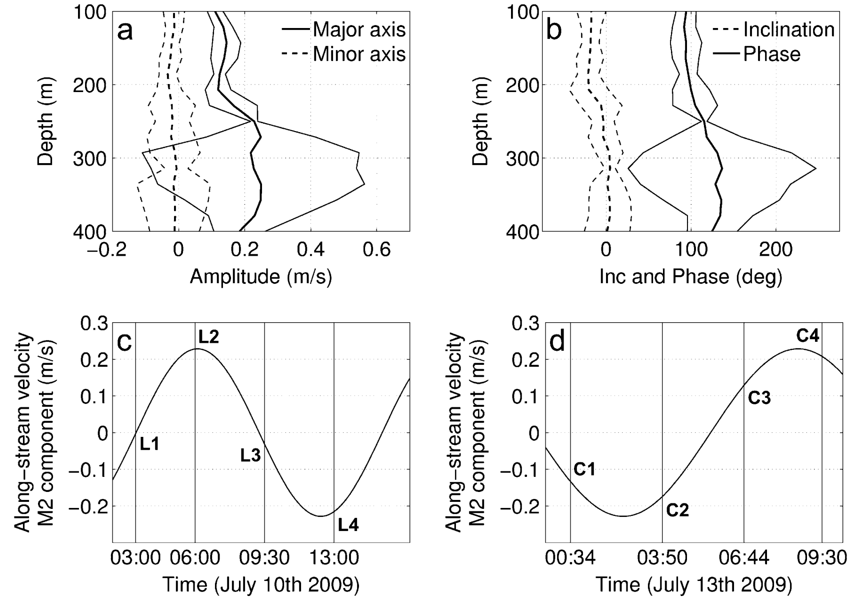


**Fig. 6** M2 velocity tidal component. **a** Depth profiles of along-stream (*thick continuous line*) and cross-stream (*thick dashed line*) velocity tidal components (*thinner lines* 95% confidence intervals). **b** Greenwich phase (*thick continuous line*) and inclination (*dotted line*) of M2 tidal velocity ellipse. **c** Vertically averaged M2 along-stream velocity component between 250–350 m during along-stream two-yos; *L1–L4* middle time for each transect. **d** Vertically averaged M2 along-stream velocity component from 250–350 m during cross-stream two-yos; *C1–C4* middle time for each transect. Positive velocity values show flow toward the strait

surface layers flow east and the swift MOW heads west, although no data are available for the deepest 50 m. Low gradient Richardson numbers are associated to the highly stratified (large buoyancy frequency) MW–NACW interface (Fig. 9); again the last transect is lacking, and Richardson numbers below 350–400 m are not shown because of ADCP contamination.

In Figs. 10, 11, and 12 depicting the flow properties for each across-stream transect, C1 and C2 correspond to conditions shortly before and after ebb tide, respectively, and C3 and C4 to before and after flood tide, respectively (cf. Fig. 6). The MOW has high salinity and turbidity values, although maximum turbidity occurs on either side of the V-shaped channel (Fig. 10). The along-stream velocity field illustrates the reversal of flow with depth, most clearly along the northern margin of the channel (and despite the absence of good-quality data near the seafloor; Fig. 11). The MW–NACW interface is characterized by

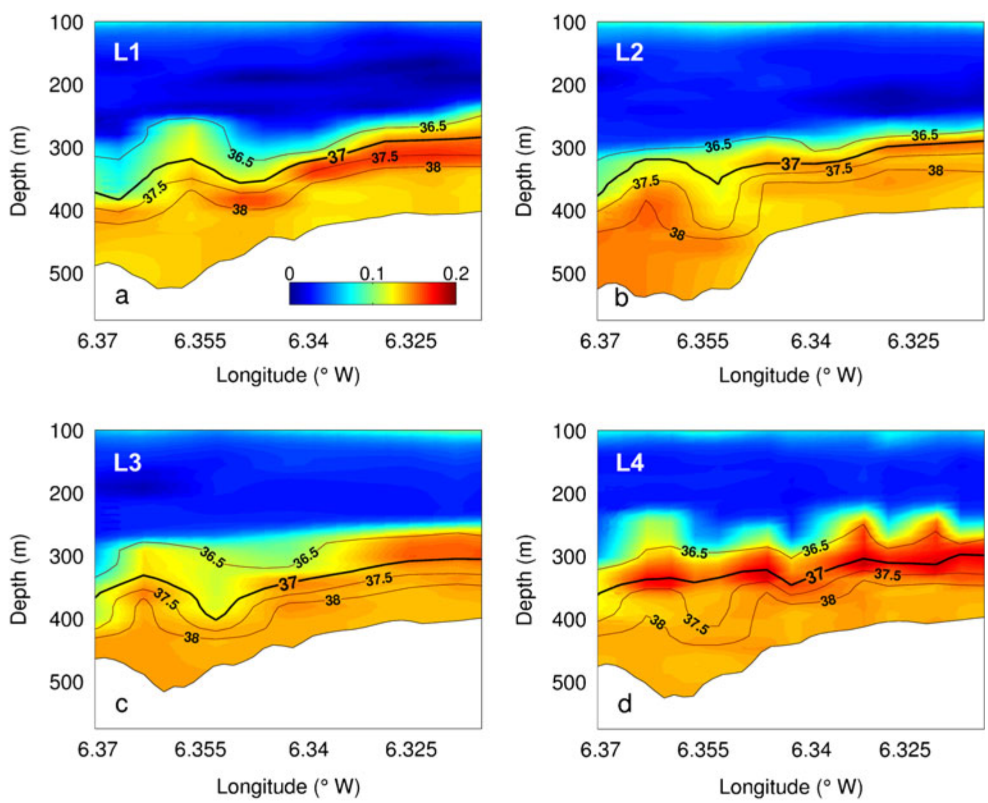


**Fig. 7** Distributions of salinity (*black contours*) and turbidity (*color*, FTU units) on along-stream short transects at four different times of the tidal cycle (see Fig. 6). *Thick solid line* 37.0 isohaline, proxy for MW–NACW interface

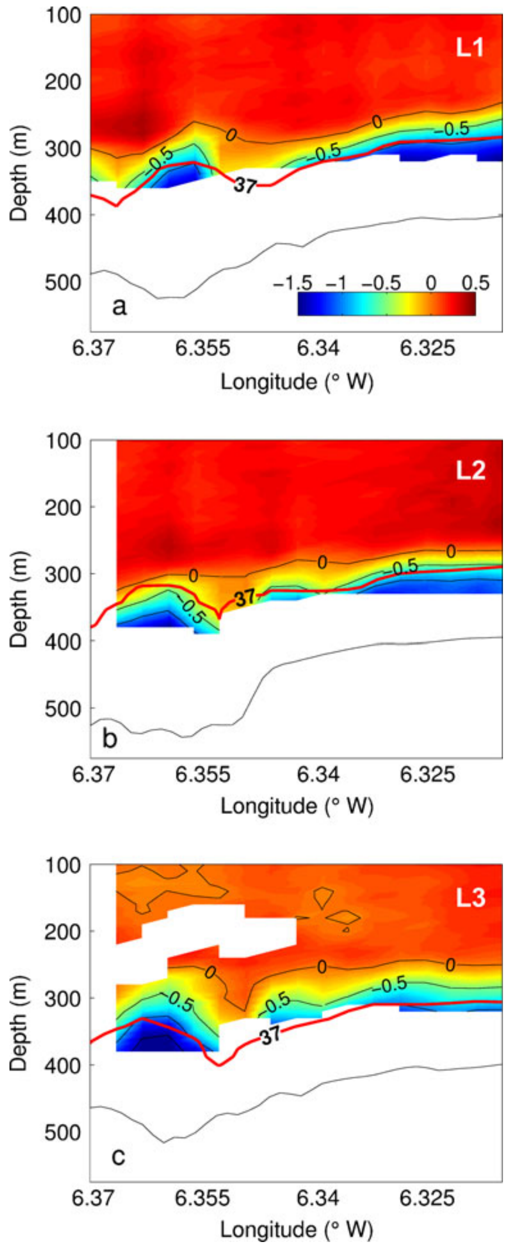


Fig. 8 Along-stream velocity (*black contours* and *color*) on along-stream short transects at three different times of the tidal cycle (see Fig. 6). *Thick solid line* 37.0 isohaline, proxy for MW–NACW interface. Positive velocities show flow toward the strait

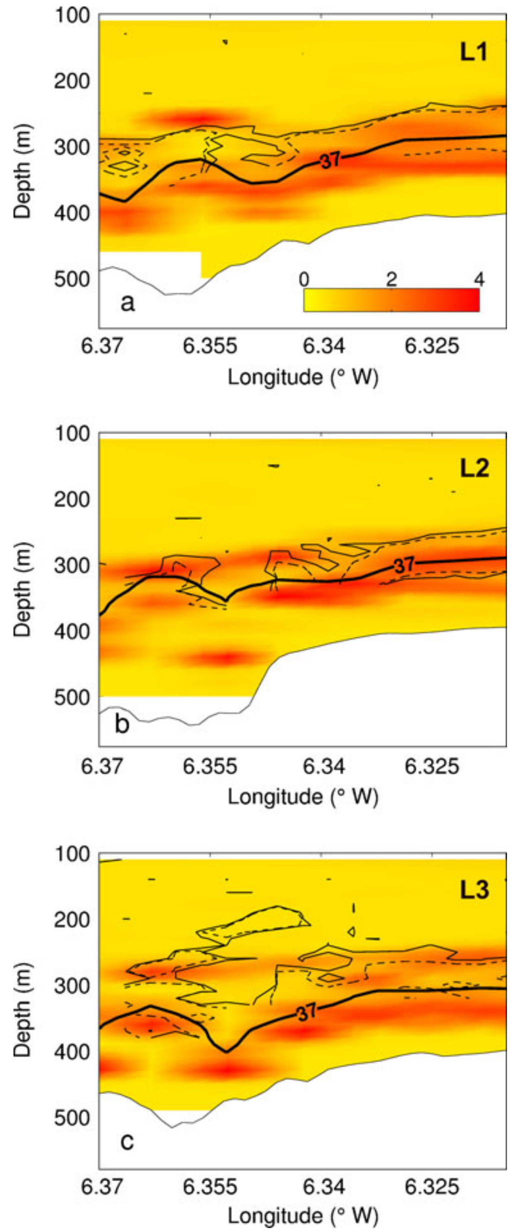


Fig. 9 Distributions of gradient Richardson number (*solid line* Ri=1, *dashed line* Ri=0.25) and squared buoyancy frequency (*color*, $10^{-4}$ cycles per hour) on along-stream short transects at three different times of the tidal cycle (see Fig. 6). *Thick solid line* 37.0 isohaline, proxy for MW–NACW interface

maximum buoyancy frequencies, except after flood (C4) when high stratification in the center of the channel reaches down to the seabed (Fig. 12).

The isohalines roughly follow the bathymetry at all times (cf. individual cross-stream short transects), although there is also some tidal modulation of the location of the salinity maximum (Fig. 10). At times C1 and C2 after maximum westward tidal velocities, the MOW wedge thins and widens, particularly toward the northern margin. At time C4 after maximum eastward velocities, the high-salinity wedge is thicker and located in the center of the channel.

The cross-stream velocity field has no clear pattern (not shown). In contrast, the along-stream flow is of a two-layer type, with the MOW reaching values exceeding 1 $ms^{-1}$ (although only along the northern margin of the channel), and the NACW flowing eastward with values locally reaching 0.3 $ms^{-1}$. The along-stream velocity contours closely follow the salinity field (Figs. 10 and 11), and the flow becomes unstable (Ri<0.25) in the pycnocline, typically for depths below 300 m (Fig. 12). These subcritical values occur in the well-stratified interface.

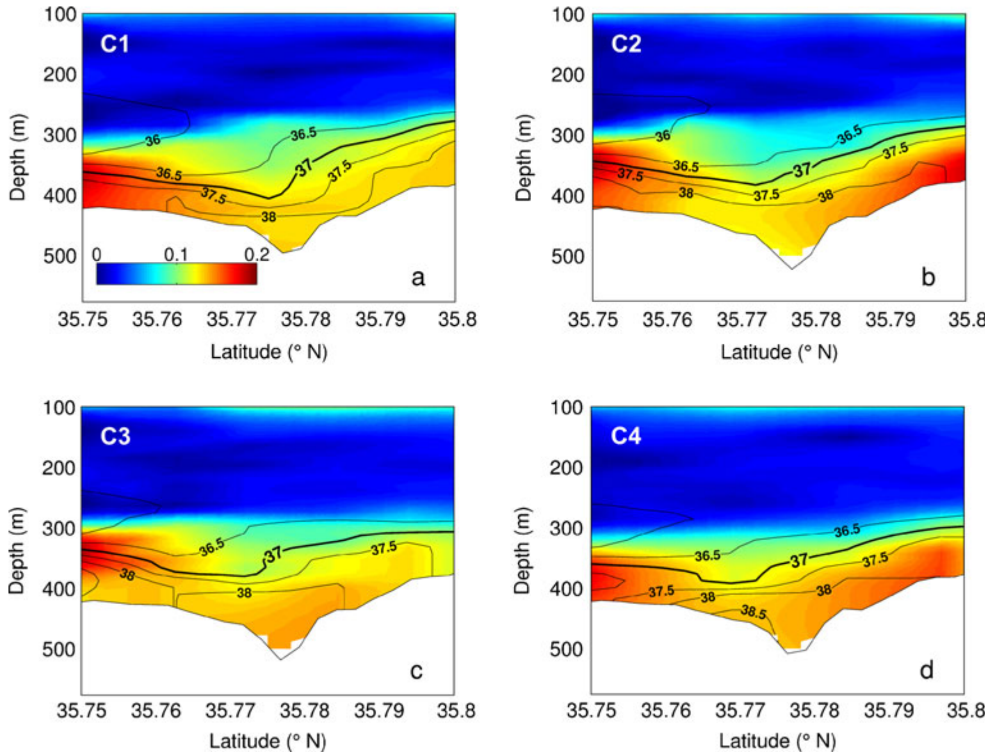


**Fig. 10** Distributions of salinity (*black contours*) and turbidity (*color*, FTU units) on cross-stream short transects at four different times of the tidal cycle (see Fig. 6). *Thick solid line* 37.0 isohaline, proxy for MW–NACW interface

## Discussion and conclusions

### MOW characteristics

The results presented above convincingly demonstrate that the bathymetry west of the Espartel Sill is responsible for both steering the MOW and determining specific sites where MOW kinetic energy becomes redistributed. The maximum salinity values (38.3) indicates that the MOW initially follows the Gibraltar Valley oriented WSW, but at 6.35°W bifurcates along two main channels, mostly the southern channel and less the northern channel (Fig. 2). Using the 37.0 isohaline as a proxy

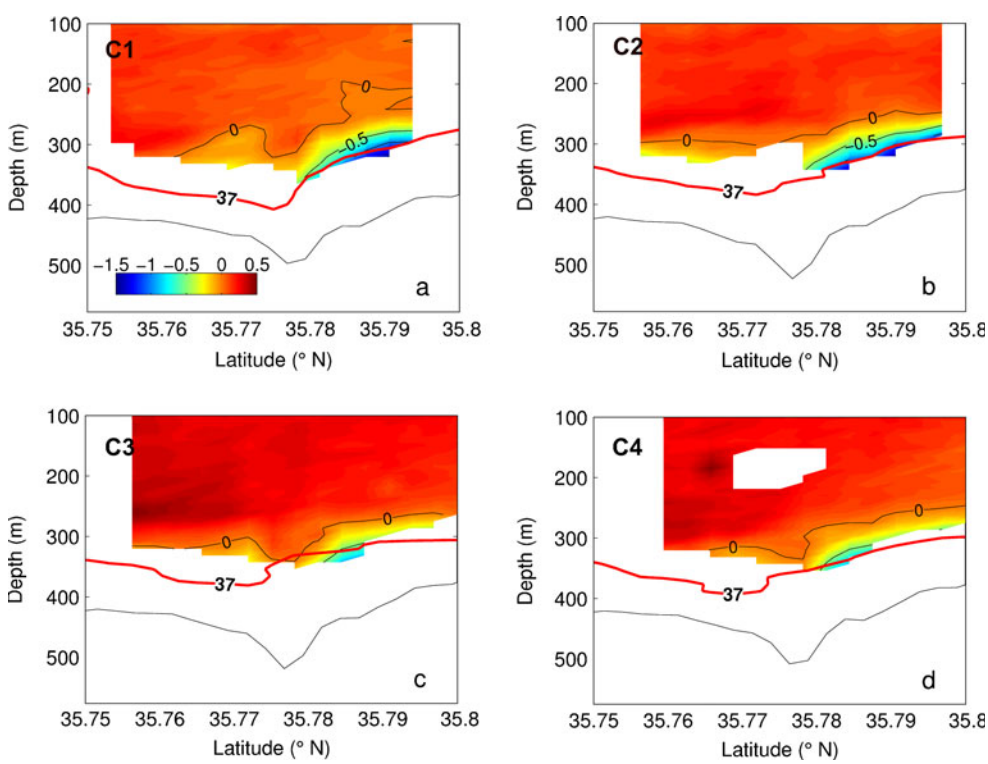


**Fig. 11** Along-stream velocity (*black contours* and *color*) on cross-stream short transects at four different times of the tidal cycle (see Fig. 6). *Thick solid line* 37.0 isohaline, proxy for MW–NACW interface. Positive values show flow toward the strait

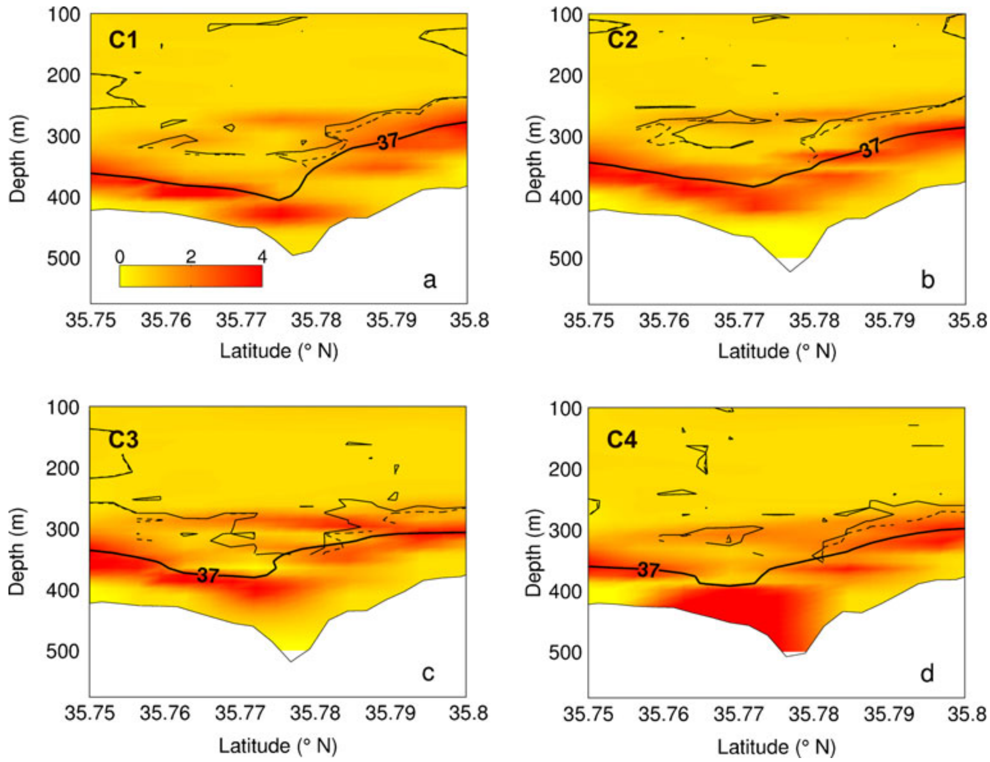


**Fig. 12** Distributions of gradient Richardson number (*solid line* Ri=1, *dashed line* Ri=0.25) and squared buoyancy frequency (*color*, $10^{-4}$ cycles per hour) on along-stream short transects at four different times of the tidal cycle (see Fig. 6). *Thick solid line* 37.0 isohaline, proxy for MW–NACW interface

for the interface between the NACW and MW, the data reveal the sinking of the MOW as it flows toward the west following the bathymetry (Fig. 4); its thickness ranges between ca. 50 and 150 m, decreasing in those areas where the bottom slope increases rapidly, and reaching maximum values over the deepest part of the channel. The salinity field in the eastern section across the MOW is symmetric with respect to the channel axis, while in the western section the isohalines rise toward the south, as do the turbidity contours (Fig. 5), indicating that the MOW is centered south of this transect.

The marked decrease in salinity corresponding to the pronounced increase in bottom depth at 6.35°W (Figs. 2 and 3) suggests the occurrence of enhanced mixing between high-salinity MW and low-salinity NACW in this area. Observations for the AS transect indeed confirm that the local increase in bottom slope induces a flow acceleration that would explain the development of large billows, typically 50 m tall and 1 km long (Fig. 7). Actually, the along-stream irregular bottom profile becomes mirrored by undulations at the MW–NACW interface. Subcritical gradient Richardson numbers (Ri<0.25) are also related to this outflow acceleration (Fig. 8), so that vertical mixing develops in the undulated and well-stratified MW–NACW pycnocline (Fig. 9).

All along-stream short transects display a two-layer structure, with high-salinity near-bottom MOW propagating westward under the NACW. MW thickness decreases in association with the pronounced increase in bottom depth at 6.34–6.35°W. While the basic characteristics of the salinity field remain similar for each transect (Fig. 7), there is considerable tidal variability in the thickness, which fluctuates by 10–50 m depending on the isopycnals considered. The data also suggest the occurrence of intermittent instabilities strongly related to the tidal phase. During the maximum outflow tide (L4), the mixing of MW (cf. salinities exceeding 37.0) displays its maximum vertical extension.

Cross-stream velocities are weak and do not exhibit any noticeable pattern along the MOW core path (not shown). In contrast, along-stream velocities closely follow the salinity pattern; MOW velocity remains negative (toward the west) during the complete tidal cycle, no MOW inversion having been observed during the cruise (Fig. 8). The gradient Richardson number is subcritical (smaller than 0.25) in large areas below 300 m, including the well-stratified interface between the MW and NACW (Fig. 9). Richardson numbers tend to be smaller west of 6.34°W, consistent with accelerated flow above the steep slopes there. High values of the buoyancy frequency occur slightly below the 37.0 isohaline, defining the sharp NACW–MW pycnocline (Fig. 9).

## Coriolis and centrifugal forces

In addition to the pressure gradient, Coriolis and centrifugal forces modify the MOW. Considering the along-stream Rossby number $\mathrm{Ro}_x$ (Eq. 5), a characteristic MOW width $L_y$=10 km (cf. Figs. 2 and 5) and maximum velocity $U$=1.4 m s$^{-1}$ result in $\mathrm{Ro}_x$=1.7. Therefore, the Coriolis force is not a principal element controlling the along-stream MOW force balance during its initial plunging stage. Setting the critical value $Ro_x$=0.1 shows that the critical velocity for $L_y$=10 km would be 0.08 m s$^{-1}$. In fact, the MOW does not reach such low values in the Gulf of Cadiz (Ambar and Howe 1979; Baringer and Price 1999).

Since $\delta = L_y/L_x$ has a small value, Eqs. 5 and 6 indicate that $Ro_y << Ro_x$. This implies that the Coriolis force has a relevant role in the cross-stream force balance. It is difficult to meaningfully estimate $\delta$, as the along-stream length scale should reflect the distance over which the dynamics remains basically unchanged, an unknown quantity. Therefore, the reverse exercise would be to set $Ro_y$=0.1, and then estimate $\delta$ for a given characteristic along-stream velocity and cross-stream distance. Specifically, for $U$=1.4 ms$^{-1}$ and $L_y$=10 km, $\delta$=0.25 or $L_y$=4.1$L_x$. This means that the Coriolis force plays an important role in the cross-stream balance at a distance only about 4 times the width of the current; using the above widths, this would occur about 40 km west of the Espartel Sill, near the western limit of the study area.

In the cross-stream balance, it is possible that the acceleration term is dominated by the curvature of the flow's path. In this case the acceleration term is $U^2/R$, $R$ being the flow's radius of curvature; Eq. 6 is replaced by $Ro_y = (U\delta^2)/(fR)$, and the cross-stream Rossby number decreases by a factor $L_y/R$. If the width of the MOW is smaller than the radius of curvature, as it happens in the study area, then the centrifugal term is negligible.

## Gravity current behavior

A relevant question is whether the MOW behaves as a gravity current as it passes the Espartel Sill. Based on characteristic values reported in García Lafuente et al. (2007), Sánchez-Román et al. (2008), and García-Lafuente et al. (2009), a total water depth $d$=360 m and MOW thickness $h$=170 m gives $\delta$=0.47; with density $\rho$= 1,029 kg m$^{-3}$ and density anomaly $\Delta\rho$=1.9 kg m$^{-3}$, Eq. 1 predicts a speed of 1.32 ms$^{-1}$. This is close to the mean maximum value reported by Sánchez-Román et al. (2008) for the Espartel Sill, 1.25 ms$^{-1}$. When $h$ decreases to 126 m ($\delta$=0.35), the outflow would increase to a maximum speed of 1.37 ms$^{-1}$, provided the density anomaly remains unchanged. Therefore, as a first approximation, the condition for maximum velocity is met by the MOW as it exits the Strait of Gibraltar at the Espartel Sill.

The rapid changes in bathymetry, and the perturbations of the interface associated with instabilities that develop at the MW–NACW interface, make it very difficult to estimate the mean thickness of the MOW layer from a single survey. In the central sector, however, the repeated short along-stream transects enabled meaningful approximations of $d$=400 m and MOW thickness $h$=100 m, so that $\delta$=0.25, again consistent with maximal speed conditions. Therefore, the observed velocity remains close to maximum velocity conditions as the MOW crosses the study area. Using the hydrographic cruise data at 6.225°W (eastern sector), 6.35°W (central sector), and 6.5°W (western sector; Figs. 3 and 5) leads to $d$=375, 450, and 500 m, and $\Delta\rho$=1.85, 1.75, and 1.65 kg m$^{-3}$, respectively. The velocity at the three locations would be 1.32, 1.41, and 1.45 ms$^{-1}$, respectively. Such an increase shortly downstream of the Espartel Sill is consistent with the results of Price et al. (1993) and Baringer and Price (1997a, b), but does not account for any tidal modulation of the flow.

Consider now the argument that the outflow always maximizes its speed, i.e., $\delta = h/d$ remains constant and close to $\delta_m$=0.35 (Eq. 1). The outflow speed varies with both the water depth and the density excess as

$$v_m = v_{m0}[(\Delta\rho/\Delta\rho_0)(d/d_0)]^{1/2} \qquad (7)$$

where $v_{m0}$ is the initial maximum speed, taken to be the case for the MOW over the Espartel Sill, and $\Delta\rho_0$ and $d_0$ respectively are the MOW initial excess density and initial water depth that lead to $v_{m0}$. Figure 13 shows two possible linear paths for the MOW in the ($\Delta\rho/\Delta\rho_0$, $d/d_0$) space, one for each of its two main cores. The path goes from the initial (1, 1) point to a final (0, $d_f/d_0$) position, where $d_f/d_0$=600 m/ 360 m=5/3 for the upper core (UC), and $d_f/d_0$=1,080 m/ 360 m=3 for the lower core (LC). This simply presupposes that the density difference will decrease linearly with depth, until it becomes zero at the final point. Hence, the depth and density excess are related: $d/d_0 = 5/3 - (2/3)(\Delta\rho/\Delta\rho_0)$ for the UC, and $d/d_0 = 3 - 2(\Delta\rho/\Delta\rho_0)$ for the LC.

Consider now a linear decrease in the density excess with distance, i.e., $x/L = (1 - \Delta\rho/\Delta\rho_0)$, where $L$=200 km is the distance between the Espartel Sill and a final point near Cape San Vicente. These considerations lead to the

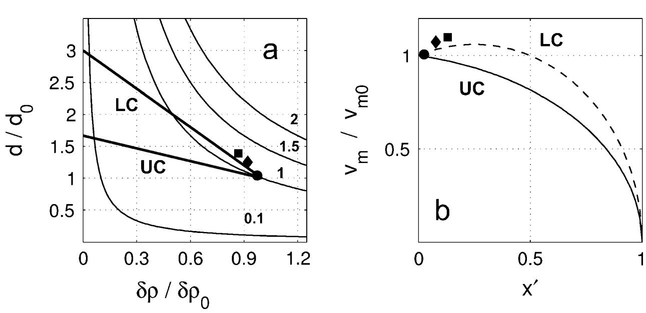


**Fig. 13** **a** Normalized maximum velocity $v_m/v_{m0}$ (*thin solid lines*) in the $(\Delta\rho/\Delta\rho_0, d/d_0)$ space: *thick solid lines* possible path for the MOW's upper core (UC) and lower core (LC) from a position (1, 1) near the Espartel Sill to a final depth-stabilized position (0, $d_f/d_0$). **b** Normalized maximum velocity $v_m/v_{m0}$, for both UC and LC, as a function of the normalized distance $x' \equiv x/L$ between the Espartel Sill and the final depth-stabilized position. *Circle*, *diamond*, *square* Values calculated using cruise data along the MOW path for depths of 375, 450, and 500 m, respectively

following final expressions for the normalized velocity as a function of the distance along its path: $v/v_{m0} = \{(\Delta\rho/\Delta\rho_0)[5/3 - (2/3)(\Delta\rho/\Delta\rho_0)]\}^{1/2}$ for the UC, and $v/v_{m0} = \{(\Delta\rho/\Delta\rho_0)[3 - 2(\Delta\rho/\Delta\rho_0)]\}^{1/2}$ for the LC, where $\Delta\rho/\Delta\rho_0 = 1 - x/L$.

It may be argued that the MW density excess should decrease very rapidly during the early plunging stage as a result of more intense mixing, i.e., a more realistic nonlinear relation between $x$ and $\Delta\rho$ could be chosen. Furthermore, the instantaneous MOW speed may differ from the above calculated maximum values because of two factors: the bottom slope, and tides. Typical mean bottom slopes are small (tan $\alpha$=0.01–0.1), so that they should lead only to minor changes in the pressure difference at the head of the gravity current. On the other hand, tidally induced flow is not negligible, with amplitudes exceeding 0.2 $\mathrm{m\,s^{-1}}$ (Fig. 6). Nevertheless, the cruise data do show good agreement with the lower-core predictions for water depth, density difference, and normalized velocity (cf. Fig. 13). In particular, the LC data predict an initial increase in velocity with distance from the Espartel Sill, consistent with the velocity data. This initial velocity increase also agrees with observations by Price et al. (1993) and Baringer and Price (1997a). Figure 13 indeed suggests that the two MOW cores will experience relatively small velocity changes until the density excess of the intruding current $\Delta\rho$ approaches zero. At this late stage along the continental slope in the northwestern Gulf of Cadiz, the MOW would find its compensating depth and the flow dynamics would no longer be that of a density-driven flow.

## Vertical motions and energy considerations

The available potential energy of the dense MOW wedge that exits the Strait of Gibraltar at depths of 200–350 m is progressively converted into mean flow kinetic energy. This enables the outflow to maintain high velocities despite the large increase in water transport resulting from entrainment of the overlying NACW (Ambar and Howe 1979; Ochoa and Bray 1991; Baringer and Price 1997a, b; Xu et al. 2007). Not all the outflow energy is transformed into the kinetic energy of the increased transport. Some energy is dissipated through turbulence in the boundary and interfacial layers (Johnson et al. 1994), and some is transformed back into potential energy through the formation of an intermediate layer with MW–NACW mixed characteristics. Some energy may also be released without mixing through the production of radiating internal waves from the undulating interface.

In the study area the velocity difference between MW and NACW is so large that Kelvin-Helmholtz-like interface billows develop, as identified by the ship's echo-sounder. The condition for this to occur is that the flow near the MW–NACW interface has to be subcritical, i.e., the excess kinetic energy of a water parcel that moves up in the water column is greater than the excess potential energy necessary to make this displacement permanent. This necessary condition is satisfied by gradient Richardson numbers smaller than a critical value of 1 (see Figs. 9 and 12). These instabilities overturn and mix large water parcels, in a diffusive process with temporal memory (Pelegrí and Sangrà 1998). This process can lead to the creation of an intermediate layer on top of the less-diluted MW layer, this potentially being the initial breakdown of the MOW as two cores that propagate into the Gulf of Cadiz at different levels and with distinct densities. However, further data are needed to verify if this mixed zone remains downstream or if it disappears in the sheared flow. The cruise observations show that this intermediate layer is yet fresher (salinities about 36.5–37.0) and the deep layer saltier (salinities >38.0) than the lower and upper MOW cores near Cape San Vicente (salinities about 37.1 and 37.4, respectively), implying that substantial vertical mixing still remains to be performed along the MOW path.

The generation of undulations at the MW–NACW interface, with a vertical scale of 50 m and horizontal scale of 1 km, appears related to accidents in the bottom morphology and vertical inversions in the potential density field (Fig. 4). The temporal scale of these Kelvin-Helmholtz-type instabilities should depend on the stratification of the flow, specifically on the large density difference between MW and NACW. This timescale is of order $N^{-1}$ (Holst et al. 1992; Pelegrí and Sangrà 1998), the buoyancy frequency being defined as in Eq. 3. Using $d\rho/dz \approx \Delta\rho/\Delta z = -1.75\ \mathrm{kg\,m^{-3}}$ per 100 m indicates that those billows developing at the MW–NACW interface are of rather short duration, no more than a few minutes.

## Erosive potential

The joint effect of high near-bottom velocities (mean kinetic energy), energetic interfacial undulations (internal wave energy), and overturning billows (turbulent kinetic energy) may increase the energy available from the flow, and facilitate sediment erosion and transport. The energy supply necessary for erosion may be expressed as bottom stress (force per unit area) multiplied by velocity (distance per unit time) in the same direction as the bottom stress, i.e., work per unit area and time, or power per unit area. Since bottom stress is proportional to the squared velocity, it means that power per unit area is proportional to velocity cubed. This leads to intermittent, highly erosive events linked to the fastest MOW velocities. A major event would occur when the MOW accelerates by the joint effect of a subcritical mean flow (e.g., the MOW thins and accelerates following a substantial increase in the bottom slope) and the westward tide component of the velocity. The frequency and intensity of these events may be seasonally or inter-annually modulated by other factors such as the evaporation–precipitation balance in the Mediterranean basin, and meteorological forcing over and at both sides of the Strait of Gibraltar (Stanton 1983; García Lafuente et al. 2007; García-Lafuente et al. 2009).

The actual MOW erosive capacity, however, would not only be a function of its velocity but also depend on the grain size and cohesion of the sediments. In this area the maximum turbidity signal is located over the two margins of the channel, in areas of high speed but away from the absolute velocity maximum located immediately over the channel bed (Fig. 10). This turbidity distribution suggests the presence of different bottom grain sizes in these sectors: the high velocities may have removed all fine-grained sediments from the center of the channel, so that the channel progressively evolves out, eroding the margins where grains of relatively small size remain and causing upstream erosion.

Contour currents are traditionally considered to flow along-slope, in near-geostrophic equilibrium and giving rise to contourite drifts; in contrast, downslope processes have been usually related to turbidity-driven flows resulting in turbiditic architectures (e.g., Chapter 15 in Kennett 1982). The nascent MOW does not share the properties of a contour current, as it moves toward deep waters along the Gibraltar Valley. It is along this central axis that a downslope erosional scour has developed (Fig. 10), as proposed by Habgood et al. (2003). The top of this indented V-shaped scour is no more than 500 m wide and penetrates about 50 m. This active scouring takes place along the southern branch of this valley, but what may be a remnant scour is visible in the apparently less active northern branch (Figs. 1 and 2).

This southern main branch reaches the open ocean before it turns north, along the Iberian Peninsula, initially no deeper than about 600 m (Baringer and Price 1999). However, it is possible that related downslope channels may have reached deeper in past climates (Llave et al. 2006, 2007). This could have occurred as a result of changes in the water balance within the Mediterranean basin (changing MW salinity and density), and variations in the total water depth at the Espartel Sill. As the speed of a gravity current is proportional to the squared root of both the total water depth and the density excess of the intruding water (Eq. 1), a scenario of maximum depth penetration would correspond to a thin (low total water depth) and yet very dense MOW. The high-density anomaly guarantees the possibility of reaching far and deep, but this has to occur through a relatively slow (therefore thin) current that undergoes little vertical mixing.

In conclusion, the findings show that the MOW interacts with the underlying bottom topography in a complex manner. Through its slope and shape characteristics, the seabed is responsible for steering and mixing the MOW, thereby defining its three-dimensional trajectory. In turn, MOW characteristics—e.g., erosive potential—control the slow evolution of the bathymetry. This two-way interaction possibly results in a meta-stable system, the flow and bottom variables remaining within a limited range of values. Theoretical, observational, and numerical studies are required to further characterize the key parameters controlling the stability of this system.

**Acknowledgements** The authors are deeply grateful to all aboard the R/V García del Cid, in particular Captain Eduardo Otal and technicians José Antonio Pozo, Maribel Lloret and Joaquín Salvador, as well as Mikhail Emelianov and Sam Kelly for their help in gathering data during the cruise. The authors are also very grateful to Gemma Ercilla and two anonymous reviewers for many useful comments. Funding for this work comes from the Ministerio de Ciencia e Innovación, Spain, through project MOC2 (CTM2008-06438-C02-01), project INGRES (CTM2006-02326), and two complementary actions (CTM2008-03422-E/MAR and CTM2009-05810-E/MAR); funding also comes from the US National Science Foundation (grants OCE-0825287 and OCE-0825297).

## References

Ambar I, Howe MR (1979) Observations of the Mediterranean outflow I. Mixing in the Mediterranean outflow. Deep Sea Res A 26:535–554

Ambar I, Armi L, Bower A, Ferreira T (1999) Some aspects of time variability of the Mediterranean water off south Portugal. Deep Sea Res I 46:1109–1136

Baraza J, Ercilla G, Nelson CH (1999) Potential geologic hazards on the eastern Gulf of Cadiz slope (SW Spain). Mar Geol 155:191–215

Baringer MO, Price JF (1997a) Mixing and spreading of the Mediterranean outflow. J Phys Oceanogr 27:1654–1677

Baringer MO, Price JF (1997b) Momentum and energy balance of Mediterranean outflow. J Phys Oceanogr 27:1678–1692

Baringer MO, Price JF (1999) A review of the physical oceanography of the Mediterranean outflow. Mar Geol 155:63–82

Benjamin TB (1968) Gravity current and related phenomena. J Fluid Mech 31:209–248

Borenäs KM, Wahlin AK, Ambar I, Serra N (2002) The Mediterranean outflow splitting—a comparison between theoretical models and CANIGO data. Deep Sea Res II 49:4195–4205

Bower AS, Serra N, Ambar I (2002) Structure of the Mediterranean Undercurrent and Mediterranean Water spreading around the southwestern Iberian Peninsula. J Geophys Res 107:3161–3179

Bryden HL, Stommel HM (1984) Limiting processes that determine basic features of the circulation in the Mediterranean Sea. Oceanol Acta 7:289–296

Candela J, Beardsley RC, Limeburner R (1990) Removing tides from ship-mounted ADCP data, with application to the Yellow Sea. In: Appell GF, Curtin TB (eds) Proc IEEE 4th Working Conf Current Measurements. Institute of Electrical and Electronics Engineers, New York, pp 258–266

García M, Hernández-Molina FJ, Llave E, Stow DAV, León R, Fernández-Puga MC, Díaz del Río V, Somoza L (2009) Contourite erosive features caused by the Mediterranean Outflow Water in the Gulf of Cadiz: quaternary tectonic and oceanographic implications. Mar Geol 257:24–40

García Lafuente J, Sánchez Román A, Díaz del Río G, Sannino G, Sánchez Garrido JC (2007) Recent observations of seasonal variability of the Mediterranean outflow in the Strait of Gibraltar. J Geophys Res 112:C10005. doi:10.1029/2006JC003992

García-Lafuente J, Delgado J, Sánchez Román A, Soto J, Carracedo L, Díaz del Río G (2009) Interannual variability of the Mediterranean outflow observed in Espartel Sill, western Strait of Gibraltar. J Geophys Res 114:C10018. doi:10.1029/2009JC005496

Habgood EL, Kenyon NH, Masson DG, Akhmetzhanov A, Weaver PPE, Gardner J, Mulder T (2003) Deep-water sediment wave fields, bottom current sand channels and gravity flow channel-lobe systems: Gulf of Cadiz, NE Atlantic. Sedimentology 50:483–510

Hernández-Molina FJ, Llave E, Stow DAV, García M, Somoza L, Vázquez JT, Lobo FJ, Maestro A, Díaz del Río V, León R, Medialdea T, Gardner J (2006) The contourite depositional system of the Gulf of Cadiz: a sedimentary model related to the bottom current activity of the Mediterranean outflow water and its interaction with the continental margin. Deep Sea Res II 53:1420–1463

Holst SE, Koseff JR, Ferziger JH (1992) A numerical study of the evolution and structure of homogeneous stable stratified sheared turbulence. J Fluid Mech 237:499–539

Johnson GC, Lueck RG, Sanford TB (1994) Stress on the Mediterranean outflow plume: Part II. Turbulent dissipation and shear measurements. J Phys Oceanogr 24:2084–2092

Kennett JP (1982) Marine geology. Prentice-Hall, Englewood Cliffs

Kenyon NH, Belderson RH (1973) Bed forms of the Mediterranean undercurrent observed with side-scan sonar. Sediment Geol 9:77–99

León R, Somoza L, Medialdea T, Hernández-Molina FJ, Vázquez JT, Díaz-del-Río V, González FJ (2010) Pockmarks, collapses and blind valleys in the Gulf of Cádiz. Geo Mar Lett 30(3/4):231–247. doi:10.1007/s00367-009-0169-z

Llave E, Schönfeld J, Hernández-Molina FJ, Mulder T, Somoza L, Díaz del Río V, Sánchez-Almazo I (2006) High-resolution stratigraphy of the Mediterranean outflow contourite system in the Gulf of Cadiz during the late Pleistocene: the impact of Heinrich events. Mar Geol 227:241–262

Llave E, Hernández-Molina SDAV, Fernández-Puga MC, García M, Vázquez JT, Maestro A, Somoza L, Díaz del Río V (2007) Reconstructions of the Mediterranean Outflow Water during the Quaternary based on the study of changes in buried mounded drift stacking pattern in the Gulf of Cadiz. Mar Geophys Res 28:379–394

Madelain F (1970) Influence de la topographie du fond sur l'écoulement méditerranéen entre le Détroit de Gibraltar et le Cap Saint-Vincent. Cahiers Océanogr 22:43–61

Mulder T, Voisset M, Lecroart P, Le Drezen E, Gonthier E, Hanquiez V, Faugères J-C, Habgood E, Hernandez-Molina FJ, Estrada F, Llave-Barranco E, Poirier D, Gorini C, Fuchey Y, Voelker A, Freitas P, Lobo Sanchez F, Fernandez LM, Kenyon NH, Morel J (2003) The Gulf of Cádiz: an unstable giant contouritic levee. Geo Mar Lett 23(1):7–18. doi:10.1007/s00367-003-0119-0

Nelson CH, Baraza J, Maldonado A, Rodero J, Escutia C, Barber JH Jr (1999) Influence of the Atlantic inflow and Mediterranean outflow currents on Late Quaternary sedimentary facies of the Gulf of Cadiz continental margin. Mar Geol 155:99–129

Ochoa J, Bray NA (1991) Water mass exchange in the Gulf of Cádiz. Deep Sea Res 38:S465–S503

Pawlovicz R, Beardsley B, Lentz S (2002) Classical tidal harmonic analysis including error estimates in MATLAB using T_TIDE. Comput Geosci 28:929–937

Pelegrí JL (1988) Tidal fronts in estuaries. Estuar Coast Shelf Sci 27:45–60

Pelegrí JL, Sangrà P (1998) A mechanism for layer formation in stratified geophysical flows. J Geophys Res 103:30679–30693

Price JF, Baringer MO, Lueck RG, Johnson GC, Ambar I, Parrilla G, Cantos A, Kennelly MA, Sanford TB (1993) Mediterranean outflow mixing and dynamics. Science 259:1277–1282

Sánchez-Román A, Criado-Aldeanueva F, García-Lafuente J, Sánchez JC (2008) Vertical structure of tidal currents over Espartel and Camarinal sills, Strait of Gibraltar. J Mar Syst 74:120–133

Serra N, Ambar I, Kase RH (2005) Observations and numerical modelling of the Mediterranean outflow splitting and eddy generation. Deep Sea Res II 52:383–408

Stanton BR (1983) Low frequency variability in the Mediterranean outflow west of Gibraltar. Deep Sea Res 30:743–761

Van Gastel P, Pelegrí JL (2004) Estimates of gradient Richardson numbers from vertically smoothed data. Sci Mar 68:459–482

Xu X, Chassignet EP, Price JF, Özgökmen TM, Peters H (2007) A regional modeling study of the entraining Mediterranean outflow. J Geophys Res 112:C12005. doi:10.1029/2007JC004145

Zenk W (1975) On the Mediterranean outflow west of Gibraltar. Meteor Forsch Ergebnisse A 16:23–34

Zenk W, Armi L (1990) The complex spreading patterns of Mediterranean water off the Portuguese continental slope. Deep-Sea Res 37:1805–1823

Zitellini N, Gràcia E, Matias L, Terrinha P, Abreu MA, DeAlteriis G, Henriet JP, Dañobeitia JJ, Masson DG, Mulder T, Ramella R, Somoza L, Diez S (2009) The quest for the Africa-Eurasia plate boundary west of the Strait of Gibraltar. Earth Planet Sci Lett 280:13–50